Evaluation of the Surface Wind Field over Land in WRF Simulations of Hurricane Wilma (2005). Part II: Surface Winds, Inflow Angles, and Boundary Layer Profiles

DAVID S. NOLAN,[a] BRIAN D. MCNOLDY,[a] JIMMY YUNGE,[a] FORREST J. MASTERS,[b] AND IAN M. GIAMMANCO[c,d]

[a] *Rosenstiel School of Marine and Atmospheric Science, University of Miami, Miami, Florida*
[b] *Engineering School of Sustainable Infrastructure and Environment, University of Florida, Gainesville, Florida*
[c] *Insurance Institute for Business and Home Safety, Richburg, South Carolina*
[d] *National Wind Institute, Texas Tech University, Lubbock, Texas*

(Manuscript received 17 June 2020, in final form 18 November 2020)

ABSTRACT: This is the second of a two-part study that explores the capabilities of a mesoscale atmospheric model to reproduce the near-surface wind fields in hurricanes over land. The Weather Research and Forecasting (WRF) Model is used with two planetary boundary layer parameterizations: the Yonsei University (YSU) and the Mellor–Yamada–Janjić (MYJ) schemes. The first part presented the modeling framework and initial conditions used to produce simulations of Hurricane Wilma (2005) that closely reproduced the track, intensity, and size of its wind field as it passed over South Florida. This part explores how well these simulations can reproduce the winds at fixed points over land by making comparisons with observations from airports and research weather stations. The results show that peak wind speeds are remarkably well reproduced at several locations. Wind directions are evaluated in terms of the inflow angle relative to the storm center, and the simulated inflow angles are generally smaller than observed. Localized peak wind events are associated with vertical vorticity maxima in the boundary layer with horizontal scales of 5–10 km. The boundary layer winds are compared with wind profiles obtained by velocity–azimuth display (VAD) analyses from National Weather Service Doppler radars at Miami and Key West, Florida; results from these comparisons are mixed. Nonetheless the comparisons with surface observations suggest that when short-term hurricane forecasts can sufficiently predict storm track, intensity, and size, they will also be able to provide useful information on extreme winds at locations of interest.

KEYWORDS: Boundary layer; Hurricanes/typhoons; Mesoscale models; Model evaluation/performance

1. Introduction

This is the second of a two-part study on how well a mesoscale model can reproduce, and perhaps even forecast, the surface wind field of a hurricane over land. Beyond the accuracy of hurricane track, intensity (defined as the maximum 1-min average surface wind associated with the storm), and even the size of the wind field, this study focuses on the capability of such simulations to reproduce the time history of sustained winds at fixed locations. Our case study is based on the passage of Hurricane Wilma (2005) over South Florida on 24 October 2005.

Nolan et al. (2021, hereinafter Part I) describes how two simulations were produced using the Weather Research and Forecasting (WRF) Model. Each used an outer domain with 9-km grid spacing and two vortex-following nested grids with 3- and 1-km grid spacings, and both use 60 vertical levels. The simulations were initialized from Global Forecast System "final" (FNL) analyses 27 h before landfall, but with the intensity, size, and initial location of the hurricane vortex modified so as to reproduce the National Hurricane Center "best track" analyses of Hurricane Wilma as closely as possible, particularly during the time over land. The two simulations used different planetary boundary layer parameterizations. One used the Yonsei University scheme of Hong et al. (2006), and hereinafter this simulation is referred to as FinalYSU. The other used the Mellor–Yamada–Janjić scheme described in Janjić (1994), and hereinafter is referred to as FinalMYJ.

Part I shows that both simulations reproduce the track and intensity and the size of the wind field remarkably well (see e.g., Figs. 2, 3, and 6 of Part I). The simulated intensities (peak 1-min winds at 10-m height) match the best-track analyses very closely. The centers of the simulated storms make landfall 15–20 km too far south and about 30 min later than the actual Wilma, but the simulated tracks come closer to the observed track (although still behind by about 30 min) as the storm moved across the peninsula. The sizes of the simulated wind fields, both in terms of the radius of maximum winds (RMW) and the radial extent of tropical storm-force winds, also match well with the wind field analyses provided by H*WIND (Powell et al. 1998) and the Tropical Cyclone Surface Wind Analyses (TCSWA) of Knaff et al. (2011, 2015).

Part I also noted that the ratios of the near-surface tangential wind V_t to radial wind (V_r) in the simulations and the aforementioned analyses are fairly similar over water but have some greater differences over land, especially in comparison with the H*WIND analyses. This ratio is defined by the inflow angle $\alpha = \arctan(-V_r/V_t)$ and provides another way to evaluate the realism of the low-level wind field in a simulated (or forecast) hurricane (Zhang et al. 2015; Wang et al. 2018).

In this paper, the realistic and unrealistic aspects of the simulated wind fields are demonstrated more closely by comparing time series of wind speed and direction (converted to inflow angles relative to the storm center) with in situ surface observations from Hurricane Wilma (2005). We also compare

Corresponding author: Prof. David S. Nolan, dnolan@rsmas.miami.edu

DOI: 10.1175/MWR-D-20-0201.1

the simulated boundary layer wind profiles with estimates of wind profiles computed from WSR-88D observations in Miami and Key West, Florida. A complete summary and discussion of the results from Part I and this paper are provided in the final section.

2. Datasets

To evaluate simulated winds at fixed points over land, we use observations from three sources. The first is the Automated Surface Observing System (ASOS) towers located at the airports in West Palm Beach (KPBI), Fort Lauderdale (KFLL), Miami (KMIA), and Key West (KEYW), Florida. These data were obtained from the National Centers for Environmental Information. Archived ASOS data provides 2-min mean wind speed and direction every 1 min that are measured at or very close to 10-m height.

We also compare to observations from the Florida Coastal Monitoring Program (FCMP) mobile towers that were deployed in advance of Hurricane Wilma. These towers recorded wind speed and direction at 10-m height every 0.1 s (10 Hz). Details on the deployments, instruments, and data processing are found in Masters et al. (2010) and Balderrama et al. (2011). We use data from towers T0, T1, T2, and T3. Their locations are shown in Fig. 1.

To evaluate the winds above the surface layer, we use vertical profiles of wind speed computed from velocity–azimuth display (VAD) analyses (Browning and Wexler 1968) of Doppler radar wind observations taken by the WSR-88Ds near Miami (KAMX) and Key West (KBYX). These analyses were presented by Giammanco et al. (2013; hereinafter G13) as part of a larger study of boundary layer winds in 14 landfalling hurricanes from 1996 to 2008; here we are using the data from the Wilma landfall. The G13 dataset provide estimates of wind speed and direction at altitudes of 65, 135, 198, 268, 331, 401, 735, and 1065 m at KAMX (location shown in Fig. 1) and at 35, 105,168, 238, 301, 375, 705, and 1035 m at KBYX. The KBYX radar is located at the Naval Air Station on Boca Chica Key, 7 km east-northeast of KEYW.

3. Wind swaths

A wind swath shows the peak wind experienced at each location on a map over the course of a storm and is an efficient way to summarize the potential impact of a landfall event. As discussed in Part I, prelandfall forecasts of wind swaths are not produced for the public by the National Weather Service. Wind swaths for the HWRF and HMON regional hurricane prediction models operated by the National Centers for Environmental Prediction (NCEP) are currently available via the Internet (e.g., https://www.emc.ncep.noaa.gov/gc_wmb/vxt/HWRF/index.php), but the graphics provided cover large areas and with broadly spaced contour intervals [e.g., 34–50, 50–64, 64–83 kt (1 kt $\approx$ 0.51 m s^{-1}), etc.] and are produced from hourly model output (G. Alaka 2020, personal communication). It would be difficult to ascertain the peak winds at precise locations from these images. If highly detailed wind swaths were produced from hurricane forecast models, what would they look like?

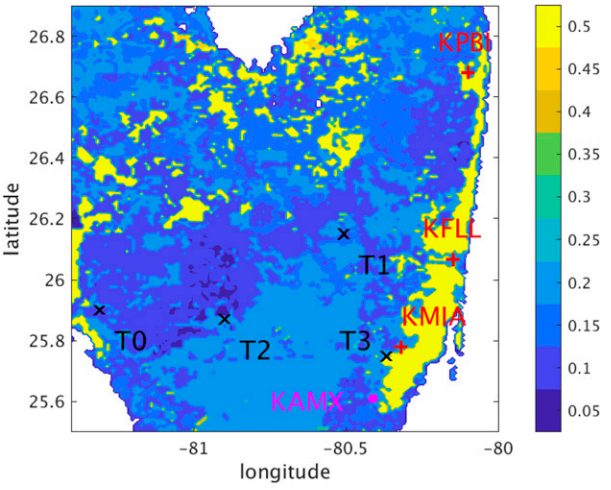

FIG. 1. Surface roughness over land in the WRF simulations (shaded colors), and locations of the airport observing towers (red plus signs), the Florida Coastal Monitoring Program weather stations (black crosses), and the Miami weather radar (magenta dots).

Figure 2 shows wind swaths over the ocean and over land for FinalYSU and FinalMYJ. These plots were generated on fixed grids with 1-km spacing in each direction. There is no spatial interpolation, because the interior grid points of the moving inner nests of WRF fall on identical locations as the nest moves (i.e., when the grid moves, almost every grid point moves to a new location that was previously occupied by another grid point, except for the leading edges of the grid). The winds here are the maximum 1-min mean winds computed from running averages of the time series produced at each swath grid point from model output every 10 s.

The overwater wind swaths show numerous curving streaks of locally increased winds, with the highest values on the right side of the storm track. As discussed in Nolan et al. (2014), these streaks show the paths of numerous mesoscale cyclonic vortices (mesovortices), with horizontal scales of 5–10 km, as they rotate around the eyewall. Each mesovortex has a local wind maximum on its right side, and the wind speed generated by a passing mesovortex is very frequently the peak wind experienced at each point. While the wind swaths are fairly similar for FinalYSU and FinalMYJ, the areal coverage of winds faster than 50 m s^{-1} is greater for FinalYSU (25 389 km^2 in Fig. 2a vs 13 518 km^2 in Fig. 2b). This may be due in part to the greater intensity of FinalYSU at this time (by 4 m s^{-1}; see Fig. 2d of Part I), but also the 50 m s^{-1} winds for FinalMYJ are more limited to the right side of the eyewall.

While less obvious, some differences can also be discerned over land. Both schemes show substantially reduced winds, with only a few locations for each exceeding 40 m s^{-1}. Here in Figs. 2c and 2d we are showing the 1-min winds without the correction to "open exposure," as discussed in section 3c of Part I. Both schemes show streaks of high wind associated with mesovortices, but for FinalMYJ the streaks are narrower and have higher wind speeds, suggesting that the mesovortices are more robust over land for FinalMYJ than FinalYSU.

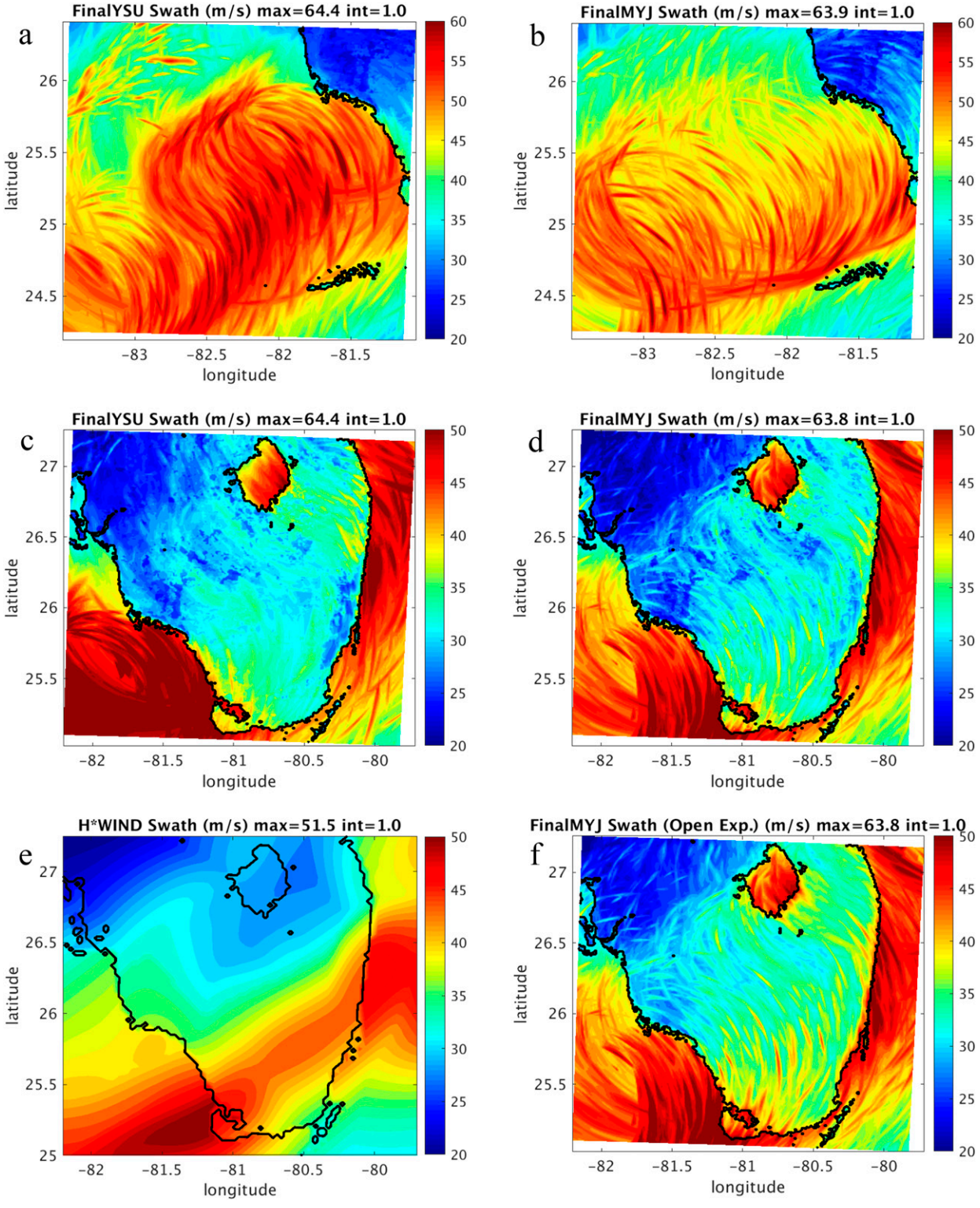

FIG. 2. Wind swaths, or maximum 1-min mean winds recorded at each point on the 1-km grid, for (a) FinalYSU before landfall, (b) FinalMYJ before landfall, (c) FinalYSU over South Florida, (d) FinalMYJ over South Florida, (e) H*WIND swath analysis, and (f) FinalMYJ corrected for open exposure.

For example, near 25.5°N and 80.5°W in Fig. 2c (FinalYSU), we can see a moderately enhanced swath of wind running from south-southwest to north-northeast, about 20 km in width, with peak wind speeds reaching 37 m s^{-1}. In contrast, near the same location in Fig. 2d (FinalMYJ), there are several swaths 5–10 km in width, with peak winds exceeding 40 m s^{-1}. The FinalYSU wind swath clearly shows the effects of increased surface roughness in the urban areas around Miami and Fort Lauderdale. Surface winds in high roughness areas are also reduced in FinalMYJ, but not as much as in FinalYSU. The areas over land with sustained hurricane force winds (34 m s^{-1} or greater) happen to be very similar (6448 and 6590 km^2) for the two cases.

Figure 3 shows snapshots of the dynamical features that create the streak patterns in the wind swaths. The times and locations of the two plots have been selected to show the mesovortices that created the wind streaks just north of West Palm Beach for FinalYSU (see Fig. 2c) and just south of West Palm Beach for FinalMYJ (see Fig. 2d). Each plot shows the vertical vorticity (color shading) and the vertical velocities with updrafts in blue contours (2 and 4 m s^{-1}) and downdrafts in white contours (1 and 2 m s^{-1}) on model level 8, which has a mean altitude of 666 m. The black contours show the 10-m wind speeds with values of 35 and 39 m s^{-1}. The trajectory of the wind speed maximum leaves a trail of locally increased winds that produce the streaks in the wind swaths. The plots show that the peak surface wind speed is on the right side of the mesovortex and lies mostly underneath a downdraft or in between a downdraft and updraft pair that is dynamically coupled to the vortex. Because the updraft/downdraft couplet creates a horizontal vorticity vector that points approximately in the direction of the flow, one can visualize the mesovortices as columnar vortices tilted in the direction of the flow, with its base at the surface trailing behind because the wind speed is reduced there.

A subjective review of these vortices using animations of the model output (not shown) finds that over land they typically exist for 5–15 min while traveling 25–35 m s^{-1}, such that the strongest ones can produce streaks in the wind swaths ranging in length from just a few km to as long as 30 km. They appear to last longer over water and also over the smoother surface of the Everglades.

The realism of these structures is difficult to assess. There are vortices of many scales in the boundary layer, cascading down to nearly isotropic turbulence, as can also be seen in large-eddy simulations of hurricanes (e.g., Zhu 2008; Rotunno et al. 2009; Stern and Bryan 2018). Several studies that resulted from extensive radar and surface-based observations taken during the landfall of Hurricane Harvey (2017) (Fernández-Cabán et al. 2019) discuss features with both similarities and differences to those shown in Fig. 3. From a dual-Doppler analysis using both National Weather Service radar and portable Doppler radar observations, Alford et al. (2019) generated local wind swaths at 500-m altitude and found streaks of enhanced wind quite similar to those that are shown in Fig. 2, which they found to be caused by individual mesovortices in the eyewall. Wurman and Kosiba (2018) show evidence for two classes of mesovortices, one that is similar in scale to those in

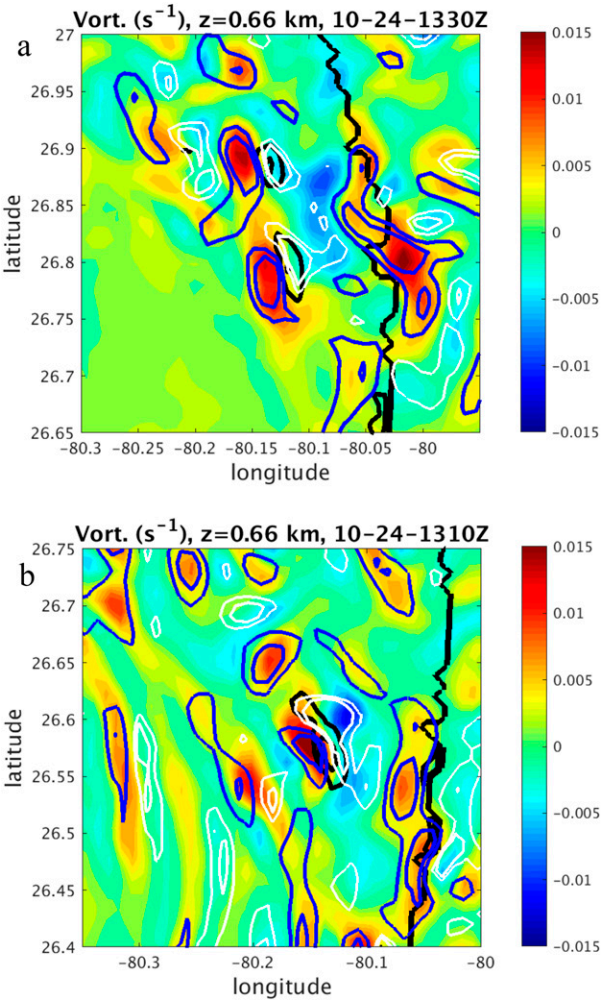

FIG. 3. Snapshots of vorticity, updraft, downdraft, and near-surface winds in the boundary layer for (a) FinalYSU at 1330 UTC and (b) FinalMYJ at 1310 UTC. Colors show vertical vorticity (s^{-1}), blue contours show vertical velocity at 2 and 4 m s^{-1}, white contours show vertical velocity at −1 and −2 m s^{-1}, and black contours show wind speeds of 35 and 39 m s^{-1}. The long, thicker black contour shows the Florida coastline near West Palm Beach.

our simulations and in Alford et al. and a smaller class of ''tornado-scale-vortices'' with horizontal scales of less than 1 km. However, they noted that only the larger mesovortices were associated with a significant increase in the 1-min wind speed; the smaller vortices increased winds locally for a few seconds.

In the case of Hurricane Wilma, the eye and the width of the eyewall at landfall were very large, generating a broad field of numerous mesovortices in the northeast through northwest quadrants of the eyewall (not shown). The vortices in our Wilma simulations appear to be rooted in the boundary layer and thus are not the dynamical equivalents of the larger mesoscale vortices frequently observed on the inner edges of hurricane eyewalls (Muramatsu 1986; Nolan and Montgomery 2002; Hendricks et al. 2012). This is supported by comparison

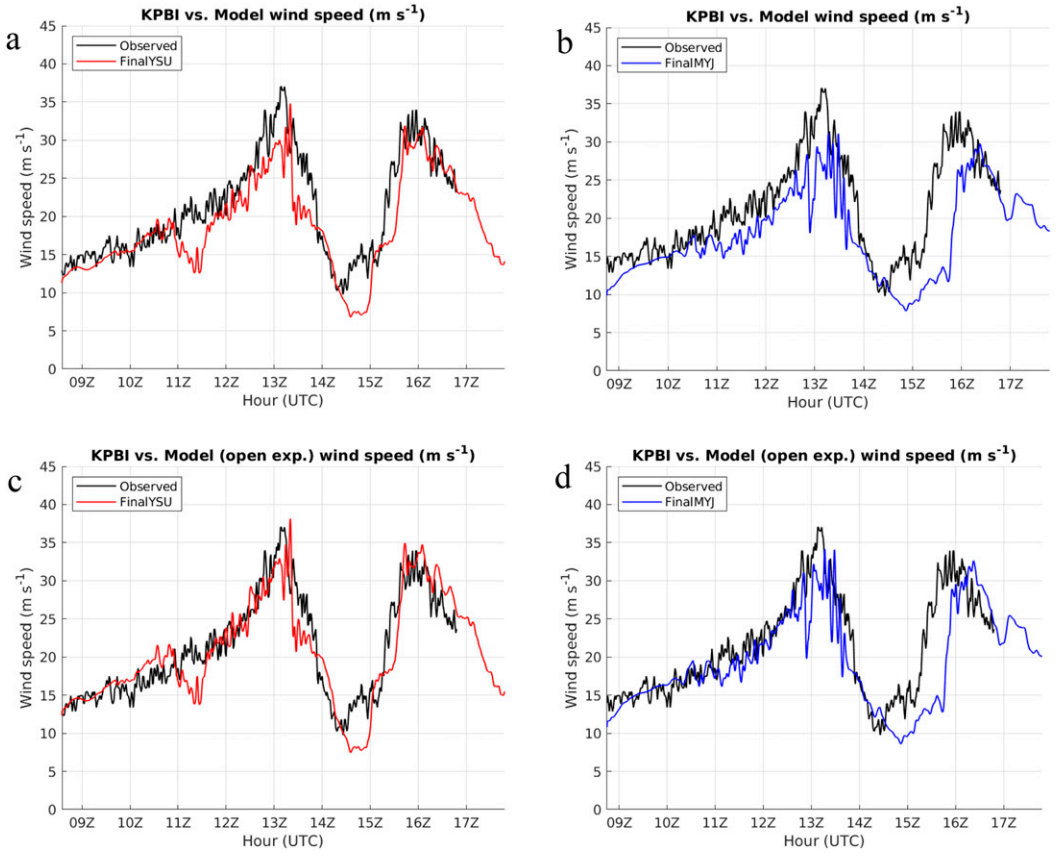

FIG. 4. Time series of 2-min mean wind speeds and simulated winds at the observing station KPBI: (a) observed wind speeds and FinalYSU; (b) observed and FinalMYJ; (c) with FinalYSU corrected for open exposure; (d) with FinalMYJ corrected for open exposure.

with the mesovortex structures observed by Wingo and Knupp (2016), which are larger in scale and have their peak vertical velocities displaced radially outward from the positive vorticity maximum, in contrast to what is shown in Fig. 3.

It is well established from observations that streamwise wind streaks and boundary layer rolls are also prevalent in the hurricane boundary layer, with cross-roll scales ranging from as little as 100 m to the depth of the boundary layer (Morrison et al. 2005; Lorsolo et al. 2008; Kosiba et al. 2013). Other than streamwise features with unrealistically large horizontal scales, as noted in Part I (see Fig. 4 of that paper), such features are not reproduced in these simulations. Unfortunately, there are insufficient observations of the near-surface, three-dimensional wind field in hurricane boundary layers to definitively say whether the low-level mesovortices shown here are accurate representations of physical processes. Rather, the purpose of this discussion is to clarify that it is these features that produce the localized areas of peak winds in the modeled wind swaths.

For some storms of historical interest, wind swaths have been produced from H*WIND analyses. This analysis for Wilma is shown in Fig. 2e. It is very different. As discussed in Part I, H*WIND analyses are calibrated to correspond to the 1-min mean winds at the surface in an environment with ''open exposure.'' Therefore, its overland wind speeds are expected to be greater than model output that has not been similarly adjusted. The differences in the H*WIND swath go well beyond this, as it shows a broad and steady swath of winds reaching 43 m s^{-1} stretching across the southern end of the peninsula. This is not surprising because H*WIND swaths are produced by advecting instantaneous analyses along the storm track (Powell and Houston 1996). For comparison, Fig. 2f shows the FinalMYJ wind swath corrected for open exposure. This swath does show some winds reaching 45 m s^{-1}, but only in the narrow areas of the aforementioned wind streaks. The H*WIND swath does not show any reduction of winds in the urban areas, nor does it show the greatly enhanced winds over Lake Okeechobee.

Because both the atmosphere and numerical simulations are highly chaotic, we cannot expect that any model could reproduce the timing and locations of the actual streaks. Rather, the simulations suggest that overland surface winds exceeding 40 m s^{-1} in Wilma probably only occurred in narrow paths in the Everglades and near the coastline, in contrast to the broad swath indicated by H*WIND. Of course, we cannot definitively judge the FinalYSU and FinalMYJ swaths as being more realistic than the H*WIND swath without additional observations. Further evidence of the realism of the simulated winds will be presented in the next section.

4. Wind speed at fixed points

a. Time series comparisons with airport observations

The locations of the ASOS stations at KPBI, KFLL, and KMIA are shown in Fig. 1 along with the surrounding roughness lengths. We mostly consider the time period from 0800 to 1800 UTC, which is when the moving 1-km nested grid covered southeastern Florida so that high-frequency data are available from the model for these locations.

Figure 4 shows time series of 2-min mean wind speeds from KPBI and from FinalYSU and FinalMYJ at the closest grid point. They both show the temporal evolution of the event quite well. FinalYSU shows the wind maximum associated with the forward portion of the eyewall, the wind minimum near the center, and the second maximum, each occurring just 10–20 min later than in reality. The FinalMYJ time series is similar, but the arrival of the back side of the eyewall is delayed another 10–20 min. Both simulations show modest negative biases for wind speeds, with the peak winds being 2–3 m s^{-1} less than observations during the storm.

This negative bias may be in part due to discrepancies in the surface roughness around the airport observations. The land use dataset (see section 2b of Part I) has roughness length $z_0 = 0.5$ m across much of the urban areas of South Florida. The less developed areas have $z_0 = 0.2$ m, and in fact this is the roughness length in the model dataset at the observing towers for all three airports. As noted in Part I, a more appropriate roughness length for "open exposure" is $z_0 = 0.03$ m. It is unlikely that any of the three stations truly have open exposure in all directions. The KPBI and KFLL towers are in the middle of each airfield and thus may be close to effectively open exposure. The KMIA tower is at the west end of the airfield, with fences and buildings to the west, but relatively open exposure to the east and south.

Figures 4c and 4d show the same time series at KPBI after correction to open exposure using Eq. (3.2) from Part I. After this adjustment, the wind speeds for both time series generally come closer to the observations. FinalYSU exceeds the peaks by about 1 m s^{-1}, while FinalMYJ still underestimates the peak wind of the front of the eyewall by 3 m s^{-1} and the second by 2 m s^{-1}. Both have minimum wind speeds during the eye that are 1–3 m s^{-1} too low.

Figure 5 shows the FinalYSU and FinalMYJ time series at KMIA and KFLL using the open exposure correction. Both simulations produce higher wind speeds than observed over most of the period. The observed winds at KFLL show two wind maxima, at 1215 and 1440 UTC, of 31 and 34 m s^{-1}, respectively. The simulations overestimate the first maximum and underestimate the second, but capture the temporal evolution very well. At KMIA, the observed wind reached nearly 31 m s^{-1} three times between 1155 and 1300 UTC. This is not followed by a secondary period of increased intensity, but rather a 1-h period of sustained winds oscillating around 25 m s^{-1}. Both simulations overestimate the first peak by 2–4 m s^{-1} and then show a temporary reduction, followed by a secondary maximum around 1415 UTC. This second maximum in FinalMYJ lasts only a few minutes and is associated with a rainband just outside of the southern edge of the eyewall. The rainbands that cause these secondary wind maxima can be seen in Figs. 4d and 4f of Part I.

Last, we consider a special case of wind speed observations from Key West International Airport (KEYW). The record of 2-min winds reported every 1 min by the ASOS station at the airport ends at 1527 UTC 23 October and does not resume until 29 October. However, observations are available from the "hourly reports" that include additional observations in some hours. These continue until 0643 UTC 24 October, with the final entry reporting a sustained wind speed of 54 kt and a recent gust to 70 kt. To make a useful comparison with model output, the wind speeds and directions from the hourly reports were linearly interpolated to 1-min intervals between 0000 and 0643 UTC, and then a running 2-min mean was computed. These are shown in comparison with the model 2-min winds in Fig. 5e. Both simulations are generally 2–3 m s^{-1} higher than the observations, with FinalYSU showing some short periods of winds 3–7 m s^{-1} higher. Since the instruments stopped reporting around the time of peak intensity, we show the simulated winds for an additional 3 h after the failure. Even accounting for their apparent high biases, both simulations suggest that the peak winds at KEYW were ultimately higher than reported.

b. Time series comparisons with the FCMP towers

The FCMP towers record wind speeds at 10 Hz from which we can compute 3-s, 1-min, and 10-min means. From the 10-s model output we can compute 1- and 10-min mean winds, although the 1-min mean model winds cannot match the real variability at that time scale (see also Fig. 6 of Nolan et al. 2014). Figure 6 (of this paper) shows wind speed data from T0 along with FinalYSU and FinalMYJ at the nearest grid point. The open exposure correction is not applied in these figures. Both simulations match the qualitative evolution of the event very closely. The 10-min winds appear to provide the most useful comparison, and from these curves we can see that FinalYSU generally overpredicts the winds at T0 by 1–4 m s^{-1} over the entire event. However, in the front eyewall the peak 1-min winds from the model are only 2 m s^{-1} greater than the peak observed 1-min winds, while during the back eyewall the peak observed 1-min wind is 3 m s^{-1} greater than FinalYSU.

For FinalMYJ, the 10-min winds are closer to the observations. The simulated 1-min winds show more variability during the front eyewall, such that peak FinalMYJ 1-min wind speeds are very similar to the observed peaks. This increased variability of the 1-min winds in FinalMYJ is associated with the greater prevalence of streamwise streaks or rolls as discussed in Part I. Interestingly, these are not as evident during the passage of the back eyewall, during which the fastest 1-min winds are observed (but not simulated).

Figure 7 shows the time series comparisons for T1, T2, and T3. For T1, both FinalYSU and FinalMYJ produced peak winds that are 5–7 m s^{-1} less than observed. As for the airports, the reason for the discrepancy at T1 could be differences in the roughness lengths in the WRF dataset and in reality. While our dataset has $z_0 = 0.12$ m at the location of T1, it was stationed adjacent to Interstate Highway 75 and was surrounded by low vegetation and swamp. Masters et al. (2010) used the observed

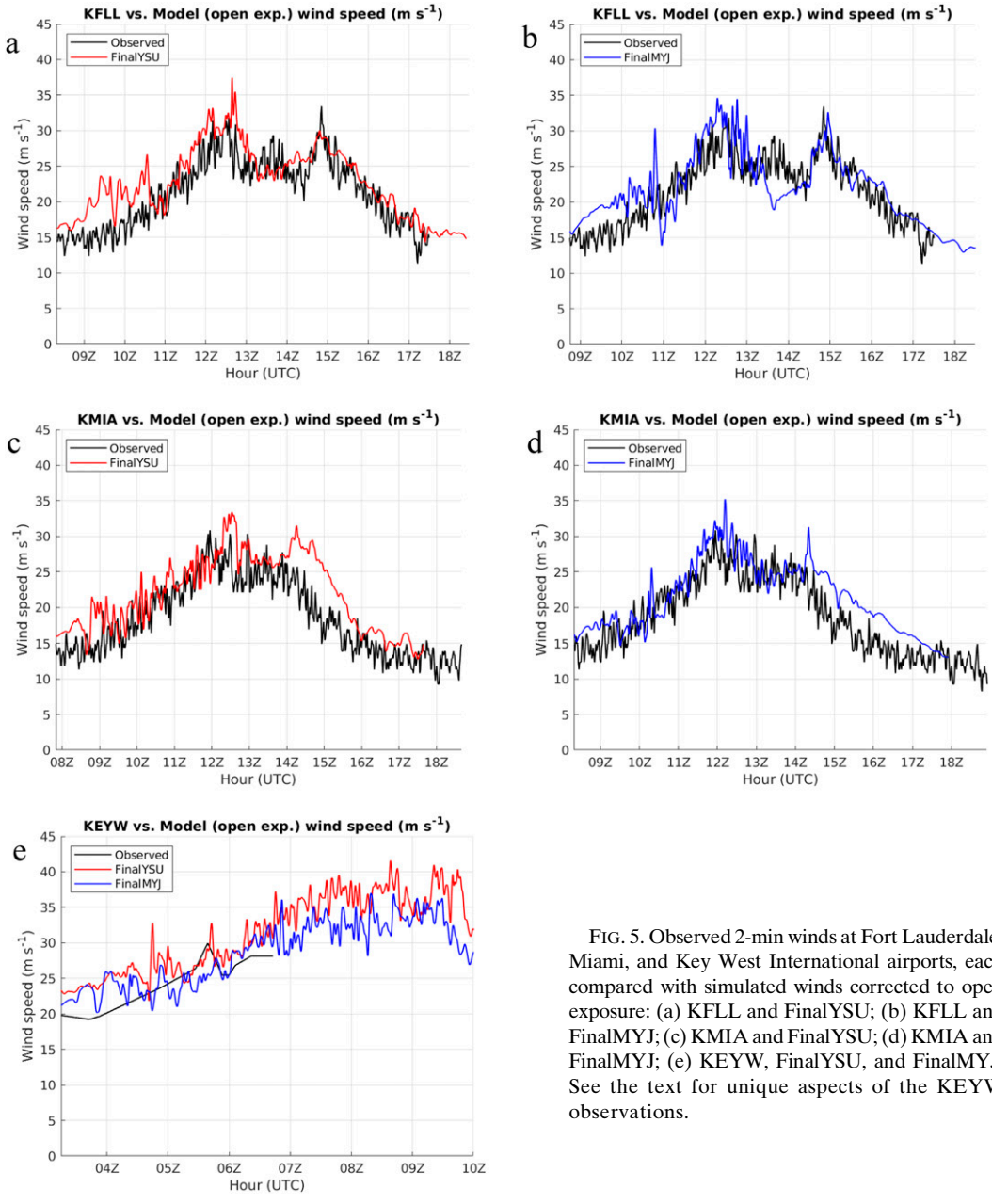

FIG. 5. Observed 2-min winds at Fort Lauderdale, Miami, and Key West International airports, each compared with simulated winds corrected to open exposure: (a) KFLL and FinalYSU; (b) KFLL and FinalMYJ; (c) KMIA and FinalYSU; (d) KMIA and FinalMYJ; (e) KEYW, FinalYSU, and FinalMYJ. See the text for unique aspects of the KEYW observations.

turbulence intensity to estimate z_0 from the data itself. Using various assumptions and subsets of the data when the wind was coming from different directions, they found values ranging from 0.003 to 0.057 m. Correcting the model output for lower roughness lengths brings the wind speeds somewhat closer to observations (not shown).

At T2 the 10-min winds are about right for FinalYSU, but during the first part of the eyewall, the 1-min winds are 5 m s^{-1} less than observed; the FinalMYJ 10- and 1-min winds are 2–3 m s^{-1} less than observed. However, both simulations come up 6 and 10 m s^{-1} short, respectively, for the 1-min winds during the back side of the eyewall. While the model has z_0 = 0.2 m at T2, roughness lengths estimated from the high-frequency data using the methods mentioned above find values ranging from 0.03 to 0.1 m, perhaps explaining some of the difference. At T3, the simulations both produce 1-min winds that are often 2–3 m s^{-1} too strong during the first maximum and then 1–2 m s^{-1} too weak during the second. Although T3 was located in the northeast corner of the Miami-Dade County Fairgrounds, the surrounding area was dense suburban sprawl. However, the model has a moderate value of z_0 = 0.2 m at T3. z_0 ~0.15 m is diagnosed at the start of the period shown in Fig. 7, decreasing to 0.03 m at the end of the period, perhaps due to the change in wind direction (from southerly to westerly) over this time.

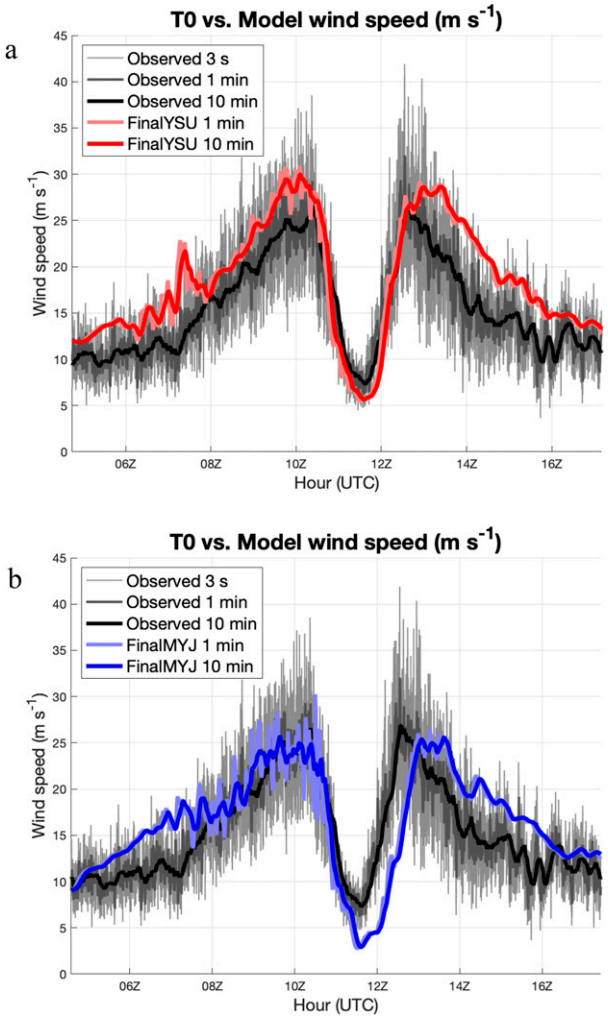

FIG. 6. Simulated wind speeds compared with high-frequency wind speeds observed at FCMP tower T0: (a) T0 and FinalYSU; (b) T0 and FinalMYJ. These winds are not corrected to open exposure.

While roughness lengths may explain some of the differences between the simulations and observations, there will always be differences, sometimes significant, when comparing simulated and observed wind speeds at specific locations.

c. *Inflow angles*

As noted in Part I, the shapes of the azimuthal-mean profiles of surface wind speed are quite similar between FinalYSU, FinalMYJ, and the two observational analyses H*WIND and TCSWA, especially from the RMW outward. Over water, the separate components V_t and V_r are also similar among the four, but, over land, H*WIND is very different. It shows drastically larger values for V_r and reduced values for V_t. These differences are highlighted by comparing the inflow angle of the low-level flow, defined as $\alpha = \arctan(-V_r/V_t)$. In contrast to some previous studies, such as Zhang and Uhlhorn (2012; hereinafter ZU12), we use the negative sign so that positive α indicates flow toward the TC center. Figure 6 in Part I shows that both the simulations and the two observational analyses, H*WIND and TCSWA, produce fairly similar α over the ocean, ranging from around 15° just inside the RMW to nearly 30° beyond $r = 200$ km. In fact, the radial profiles of α for FinalYSU and FinalMYJ are more similar to the observational composites derived from hundreds of dropsondes by ZU12 than the α profiles for H*WIND and TCSWA, which have smaller values in the range from $r = 50$ to 200 km.

The FinalYSU and FinalMYJ simulations of Wilma show spatial distributions of α that are highly asymmetric. This can be seen in Fig. 8, which shows snapshots at 0800 and 1100 UTC. Here, "wind centers" are used to define the TC center, rather than the pressure centers described in Part I. Using pressure centers for inflow angles produces asymmetric and spurious patterns of inflow angle in the eye due to the mismatch between the wind and pressure centers. Wind centers were computed by finding the location of the minimum surface wind within 50 km of the pressure center, after the wind speed field had been smoothed 50 times with a 1–1–1 filter in both directions.

The inflow angles are higher than their mean values in the front right quadrant, where the increased surface wind speed due to the storm motion leads to an increased surface stress and thus stronger radial inflow (Shapiro 1983; Kepert 2001). This result is similar to what is shown in ZU12 (see their Fig. 9), although the comparison is not perfect because they analyzed storm-relative inflow angles. For ground-relative flow, α values are even greater on the left side of this fast-moving storm because the storm motion significantly reduces V_t; this is not shown by ZU12. We find that α is lowest near the TC center, with negative values (outflow) occurring in some areas. Low and near-zero α values also occur in the right-rear quadrant of the eyewall and then behind the storm; these are also somewhat similar to the ZU12 results. The patterns of inflow angle are generally similar over land and water, although with a few differences. Over water, FinalYSU shows greater α in the front-right quadrant of the eyewall (the area extending 50–60 km north of the Florida Keys), whereas, over land, the FinalMYJ α values are larger in a broad swath from the Everglades north to Lake Okeechobee. An examination of close-up plots like those in Fig. 3 finds no systematic deviation of the flow direction as the boundary layer passes from water to land, or vice versa (not shown). This contrasts with the observational analyses of Hirth et al. (2012) and Alford et al. (2020), which both found measurable changes in the direction of the low-level flow as it passed from ocean to land.

While Hirth et al. and Alford et al. examined changes in low-level flow direction near the coastline, they did not put them in the context of inflow angles relative to the cyclone center. The airport and tower time series shown here provide an opportunity to compare directly to observed inflow angles. To compute the observed inflow angles, the best-track center positions from Pasch et al. (2006) were interpolated to 10-s intervals using cubic spline interpolation. From the simulations, the tracks were recomputed using both the pressure centroid method and the wind center method described above. The pressure and wind centers (see Fig. 2 of Part I) were then interpolated to 10-s intervals to match the high-frequency surface output. These were used to compute time series of α at the

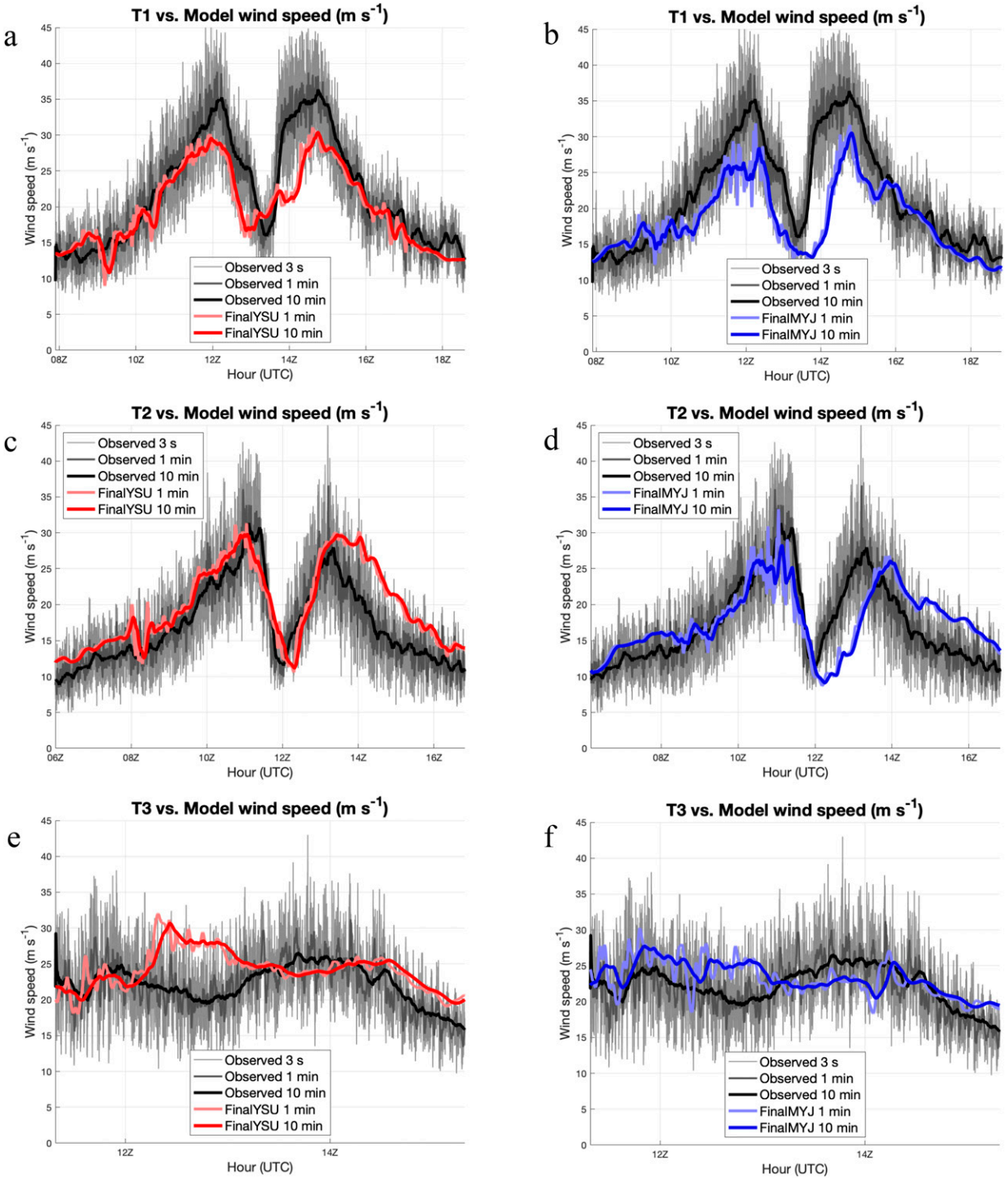

FIG. 7. As in Fig. 6 for (left) YSU and (right) MYJ, but for (a),(b) T1; (c),(d) T2; and (e),(f) T3.

airport and tower locations. Last, each time series of α was converted to 10-min running averages.

Inflow angle time series using the pressure centers for the simulated vortices showed large differences from the observed inflow angles that use the interpolated best-track centers (Landsea and Franklin 2013). As discussed in section 3a of Part I, the simulated wind centers are closer to the best-track centers than the pressure centers. Simulated α using wind centers are mostly found to be more similar to the observed α, and only these are shown here. Figure 9 shows α for KPBI,

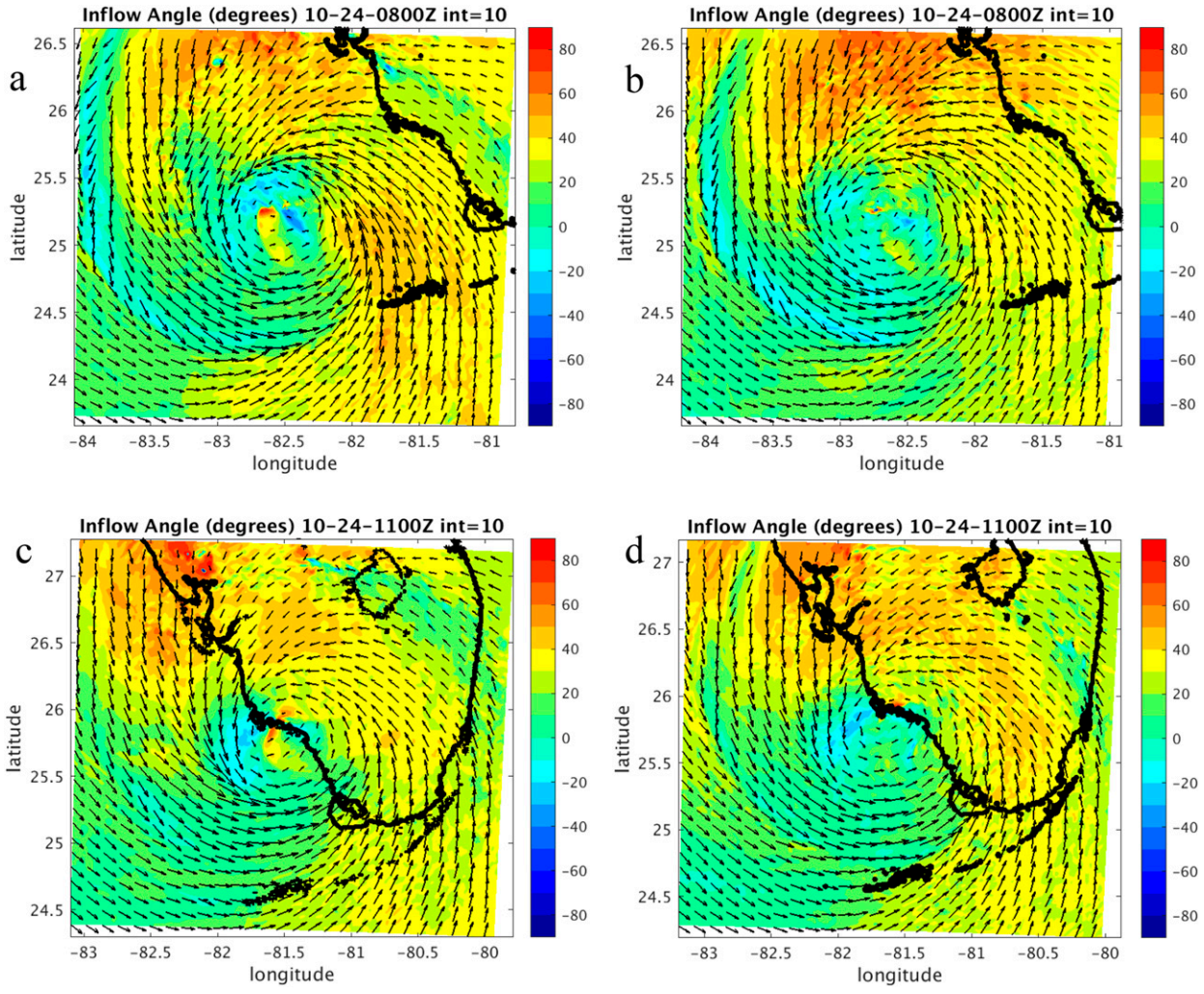

FIG. 8. Surface (10 m) wind inflow angle (shaded) and wind vectors before and then at the time of landfall: (a) FinalYSU at 0800 UTC; (b) FinalMYJ at 0800 UTC; (c) FinalYSU at 1100 UTC; (d) FinalMYJ at 1100 UTC. A wind vector that reaches to the base of its neighbor corresponds to 40 m s^{-1}.

KFLL, KMIA, and KEYW. The FinalYSU and FinalMYJ α values are very similar to each other for almost all times at all four airports. For some periods, the simulated α are very similar to observations (e.g., 0800–1100 UTC at KPBI and KFLL), whereas for other times the observed α are generally 5°–10° and occasionally 15°–20° larger (more inward). As the center passes near KPBI, the simulated wind center is even farther north than the best-track center (see Fig. 2a of Part I), so the simulated α values do not replicate the observed pattern.

The inflow angles for the FCMP towers are shown in Fig. 10. The simulated α values also range from being similar to being 10°–20° or, occasionally, 30° less than observed. From 1000 to 1200 UTC, the angles show wild oscillations at T0. Because the simulated storm tracks are 10–15 km farther south, part of the eye actually passes over T0, causing the simulated α vary wildly and to even show brief periods of outflow. This does not occur in the observations, but the large oscillations between 0900 and 1200 UTC suggest that T0 experienced passing mesovortices on the inside edge of the southern eyewall. Otherwise, the observations at all of the towers often show angles 10°–20° larger than the simulations. Across all the airports and towers, both the observed and simulated α are frequently larger than the overland profiles of azimuthal-mean α shown in Part I. This is explained by the fact that most of the stations experienced the right-front quadrant of the storm, where the inflow angles are higher than the mean.

5. Boundary layer wind profiles

a. *Comparison with low-level wind speeds derived from VAD*

Time–height diagrams of the VAD wind speed over KAMX and KBYX are shown in the top two panels of Fig. 11. The times for each individual VAD profile are indicated by the black triangles. Both figures show two temporal maxima in the boundary layer wind speed as Wilma makes its closest

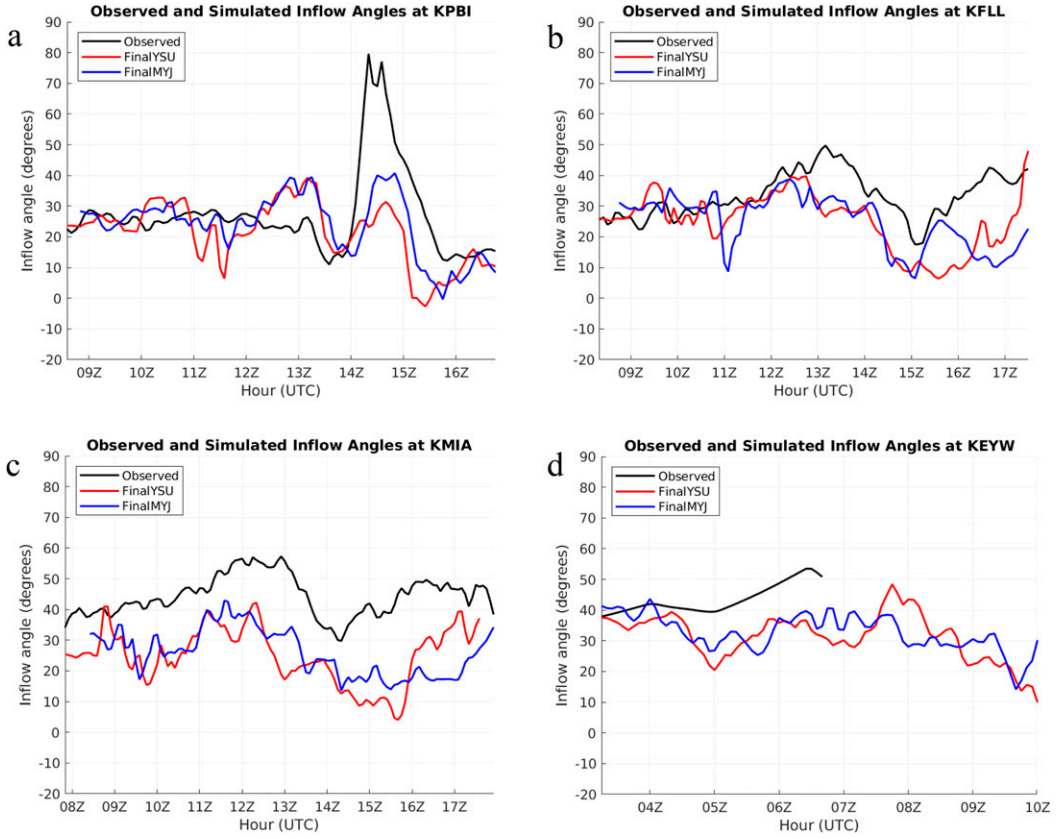

FIG. 9. Observed and simulated inflow angles at South Florida airports: (a) KPBI; (b) KFLL; (c) KMIA; (d) KEYW. See the text for unique aspects of the Key West observations.

approach to each location. The VAD wind speeds are somewhat choppy in time and, as noted in G13 for the high-wind speed cases, suggest a layer of approximately constant wind speed from 400- to 1000-m height. Without additional observations, it is not possible to say how realistic these profiles are.

VAD-like profiles of wind speed were computed from the 3-km model output at 30-min frequency and are also shown in Fig. 11. Each column of data is the average of 5×5 grid points from the 3-km output (equivalent to 15×15 grid points on the 1-km nest) centered on the grid point closest to the radar. This is somewhat like the VAD analyses of G13, which estimate the wind speed and direction from Doppler radial velocity measurements in an annulus of approximately 3–5 km around the radar. Remarkably, the FinalYSU and FinalMYJ profiles also show two temporal maxima in the total wind speed. In both cases these occur approximately 1 h later than observed, so the model data in Fig. 11 are both shown over a period 1 h later. These two peaks are also suggested by the KMIA data in Fig. 5 and the T3 data in Fig. 7.

We select times for which the local wind speed evolution and the low-level wind intensity are roughly equivalent between the VAD and the simulations. The purpose here is to compare the shapes of the wind profiles rather than the peak wind speeds either near the surface or aloft, since those are strongly influenced by differences in size, intensity, and timing of the real and simulated hurricanes. At KAMX, we use VAD data at 1112 UTC and the output from 1130 UTC for both FinalYSU and FinalMYJ. The vertical profiles are shown in Fig. 12. The near-surface wind speeds are nearly identical (by selection). The wind speed from VAD increases somewhat linearly up to 400 m and then changes to a slower rate of increase. Both FinalYSU and FinalMYJ have smoothly curved profiles, with FinalMYJ increasing more rapidly, connecting to what appears to be a transient jet at the top of the boundary layer with wind speeds reaching 65 m s^{-1} (see Fig. 11e).

At KBYX, we use the VAD profile at 0641 UTC, despite its missing data above 700 m, and compare it with 0730 UTC for both simulations. The VAD profile lies approximately on top of the FinalMYJ profile, but again it is somewhat more linear with height up to 400 m. The simulations again have smooth profiles, with less drastic increases from the surface to the upper boundary layer, perhaps because of the effectively marine environment surrounding KBYX. The model profiles are more consistent with numerous composite analyses of over-ocean wind profiles using GPS dropsondes (Zhang et al. 2011; G13; Bryan et al. 2017). When composited over many storms, the VAD wind speeds of G13 did average out to approximately logarithmic profiles (see Fig. 11a of G13). Alford et al. (2020) show composites of low-level profiles of V_t computed from VAD during the landfall of Hurricane Irene (2011), which

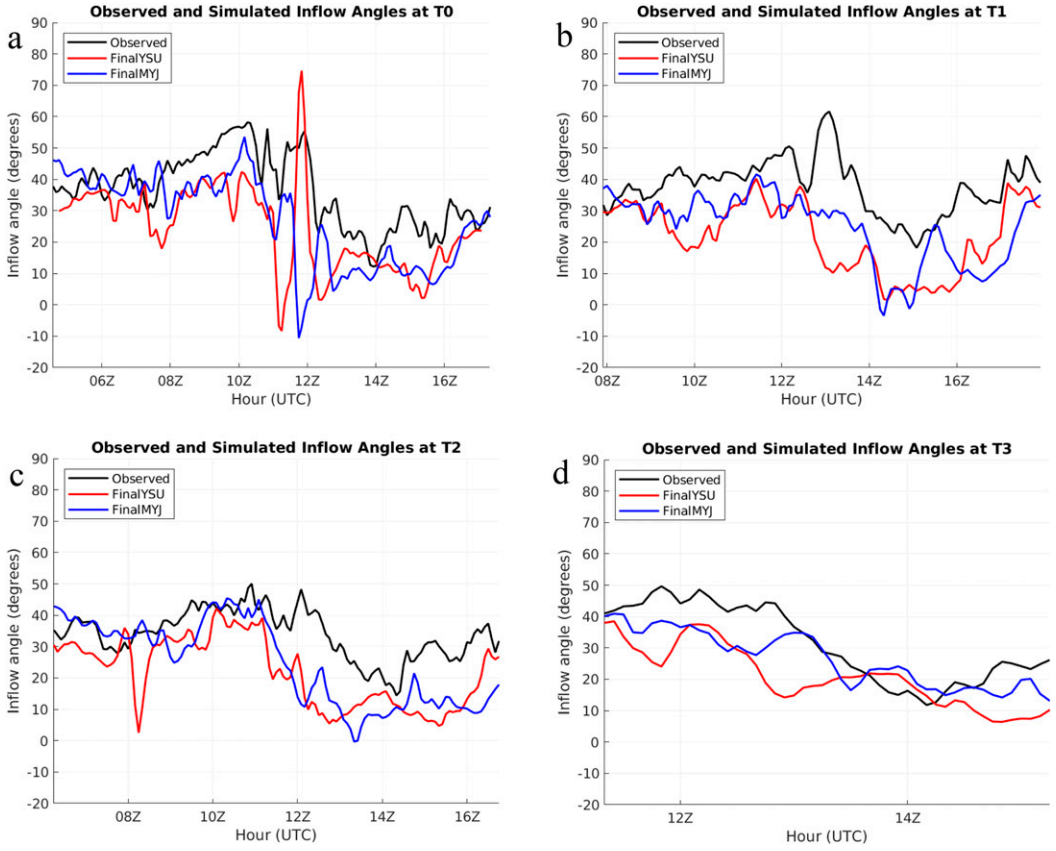

FIG. 10. Observed and simulated inflow angles at the FCMP towers: (a) T0; (b) T1; (c) T2; (d) T3.

appear to fall somewhere between linear and logarithmic. The more angular features of the VAD profiles from KAMX and KBYX during Wilma may indicate the presence of internal boundary layers or could simply be anomalous. Because of the large variation from profile to profile, the irregularity of the analyses in time, and the rapidly changing wind field of this fast-moving hurricane, compositing the VAD profiles over several analysis times did not improve the profiles or their comparisons with the model.

While the VAD wind profiles do not completely validate the simulations, they do show that the simulations reproduce the double maximum in time for the boundary layer winds experienced both at Key West and in the Miami area. This pattern is also evident from observations and simulated winds at T3 (Fig. 7) and from the simulated surface winds at KEYW (Fig. 5; observations were no longer available). The fact that both simulations reproduce this pattern is surprising, considering that they were both initialized with circular wind fields 27 h before landfall, with no additional assimilation of observations. In both simulations, the first wind peak is caused by the closest point of approach of the southeast quadrant of the eyewall, whereas the second wind peak occurs when the TC center is more directly north of the radars and is associated with an inner band just 5–10 km south of the eyewall itself (see Figs. 4d and 4f of Part 1). Strangely, at the time when the second observed VAD wind maximum occurs, the KAMX radar appears to be in between the eyewall and the first rainband (see Fig. 4b of Part 1). There is some elevated reflectivity around KAMX at this time, but it is difficult to distinguish from ground clutter.

G13 also used wind directions and 2-min estimates of center positions to decompose their winds into V_t and V_r; the results were shown in the form of composites over many storms. We did the same for G13 KAMX and KBYX data using our interpolated best-track centers. Unfortunately, the directional data are even noisier than the wind speeds, resulting in wildly varying V_t and V_r at numerous times and levels. These results are not shown.

b. *Mean wind profiles over water and land*

We more broadly compare the vertical profiles in the hurricane boundary layers produced by the YSU and MYJ schemes. In contrast to the studies by Nolan et al. (2009a,b), we do not have analyses of the boundary layer wind field with which to compare, so the purpose of this section is only to compare the two schemes with each other. The large asymmetries of the wind field, due to the fast motion of the storm and its interaction with land, make quantities averaged around the entire azimuth even less representative than usual. Therefore, we compare mean wind profiles computed across the ''east quadrant'' of the storm, defined as from −45° to +45° of a line due east of the TC centers. These quadrant means are composited from 3-km model

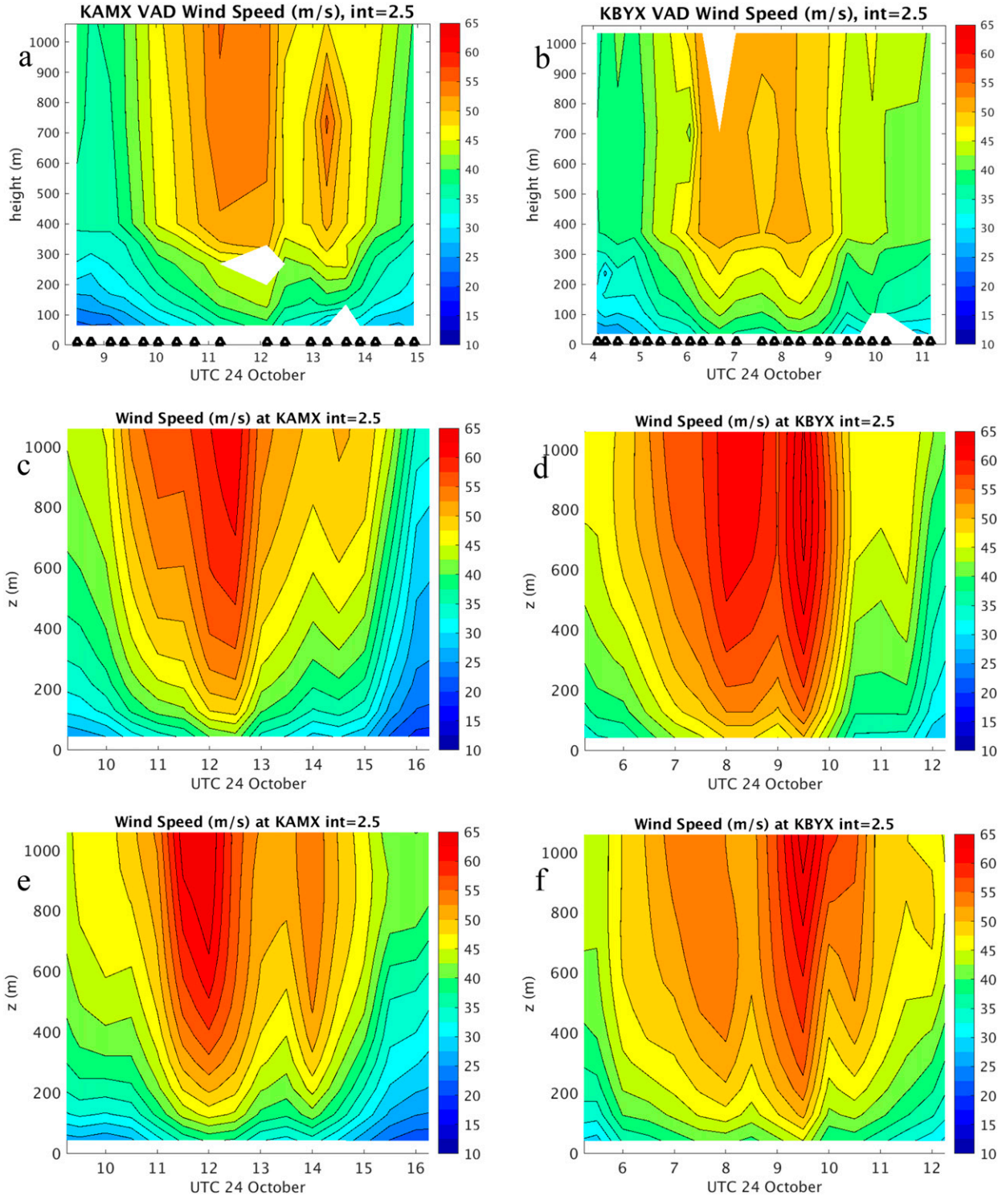

FIG. 11. Time–height profiles of wind speed at the Miami and Key West radar stations: (a) VAD profiles at KAMX; (b) VAD profiles at KBYX; (c) FinalYSU at KAMX; (d) FinalYSU at KBYX; (e) FinalMYJ at KAMX; (f) FinalMYJ at KBYX. Note that the time range is shifted 1 h later for the simulations. The analysis times for each VAD profile are indicated by the black triangles. The model data were computed on the hour and half hour.

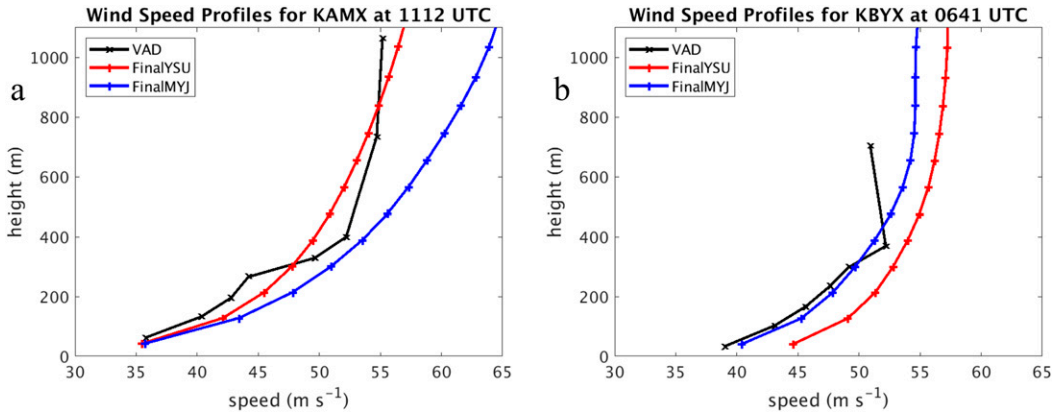

FIG. 12. Vertical profiles of wind speed from the VAD and the models at a single time above (a) KAMX and (b) KBYX. Note that the model times are actually 1130 UTC and 0730 UTC, respectively.

output from 0600 to 0730 UTC, when the east quadrant out to 2 × RMW was entirely over water, and from 1030 to 1130 UTC, when the same area was almost entirely over land.

Vertical profiles of V_t, V_r, V_{tot}, and the virtual potential temperature θ_v at the normalized radius 1.25 × RMW for the east quadrant composites are shown in Fig. 13. The upper two plots show FinalYSU and FinalMYJ over water. Each quadrant-mean wind profile is normalized by the maximum V_t occurring below 2 km. The θ_v is rescaled differently: the values shown are θ_v after subtracting its surface (2 m) value and then dividing by 5. The enlarged symbols below each profile show the 10-m values for wind and the 2-m value for θ_v, which is zero by definition of the rescaling.

With regard to the wind profiles, there are some subtle differences, but the profiles are nearly identical. This differs from the previous results of Nolan et al. (2009b), which found that the MYJ scheme produced a stronger radial inflow jet as compared to YSU. The differences may be due to small upgrades in the parameterizations in recent years, or because the previous case study was for Hurricane Isabel (2003) during the time when it was smaller, stronger, and more symmetric. The FinalYSU and FinalMYJ θ_v profiles are slightly different. However, the increased vertical gradient of θ_v for FinalMYJ is compensated by its slightly increased difference in θ_v from 2 m to the lowest model level, such that the depths of their unstable layers (where θ_v at the surface matches θ_v aloft) are nearly identical for the two schemes.

The bottom two panels show that the wind profiles have greater differences over land. FinalMYJ has a more pronounced inflow jet, and reduced values for the normalized V_t and V_{tot}, including at the surface. This is reflected in the increased inflow angle over land as shown in Fig. 8d. For both FinalYSU and FinalMYJ, the peaks in V_t and V_{tot} shift to near or above 1.5 km. This is similar to the findings of Alford et al. (2020) who also noted that, in the transition from water to land, the level of maximum V_t elevated from being within the inflow layer to being above it. The θ_v profiles are also similar, and, while both show a transition to a higher stability between the surface and the upper boundary layer, this occurs at 300 m for MYJ but at 500 m for YSU.

6. Summary and conclusions

The purpose of this two-part study was to evaluate the near-surface and boundary layer wind fields produced by mesoscale simulations of hurricanes making landfall. This evaluation is performed in the context of highly accurate simulations of the hurricane track, intensity, and size. We sought to answer the question of whether, in these ideal circumstances, a hurricane forecast model could also make usefully accurate predictions of wind speeds and direction over land. The results of this study answer these questions in the affirmative. In Part I, two WRF simulations using different boundary layer parameterizations, the YSU and the MYJ schemes, were produced, and their tracks, intensities, and sizes were validated against the best-track record and observational analyses of the size of the wind field. The YSU scheme used an option to more accurately calculate surface roughness over water in hurricane conditions. This same surface drag formula was put into the MYJ scheme, and an error in its formula for diagnosing surface wind speeds was corrected. Beyond these changes, neither scheme was modified or tuned for the purpose of predicting high-speed surface winds over land. Nonetheless, both simulations (FinalYSU and FinalMYJ) produced time series of winds at fixed points that generally agreed well with observations, and in some locations, extremely well. These results are similar to the findings of the previous work by Lin et al. (2010) who performed a similar study of Hurricane Isabel (2003).

There are some exceptions. For example, the simulated wind speeds at Tower 1 (T1) were generally 5–7 m s^{-1} lower than observed. At KMIA, KFLL, and KEYW, the simulations occasionally overpredict the wind speeds by 3–5 m s^{-1}. As discussed in Part I and in previous studies (Powell et al. 1996; Masters et al. 2010), accounting correctly for the effects of surrounding exposure on wind speed observations is a critical step in either developing a consistent analysis of a severe weather event, or in validating forecasts or simulations of an event. In our case, the land surface roughness dataset and the resolution of the model (1 km) did not accurately portray the low-roughness environments of the airport measurements and at T1. Fortunately, some of the FCMP tower sites were not in

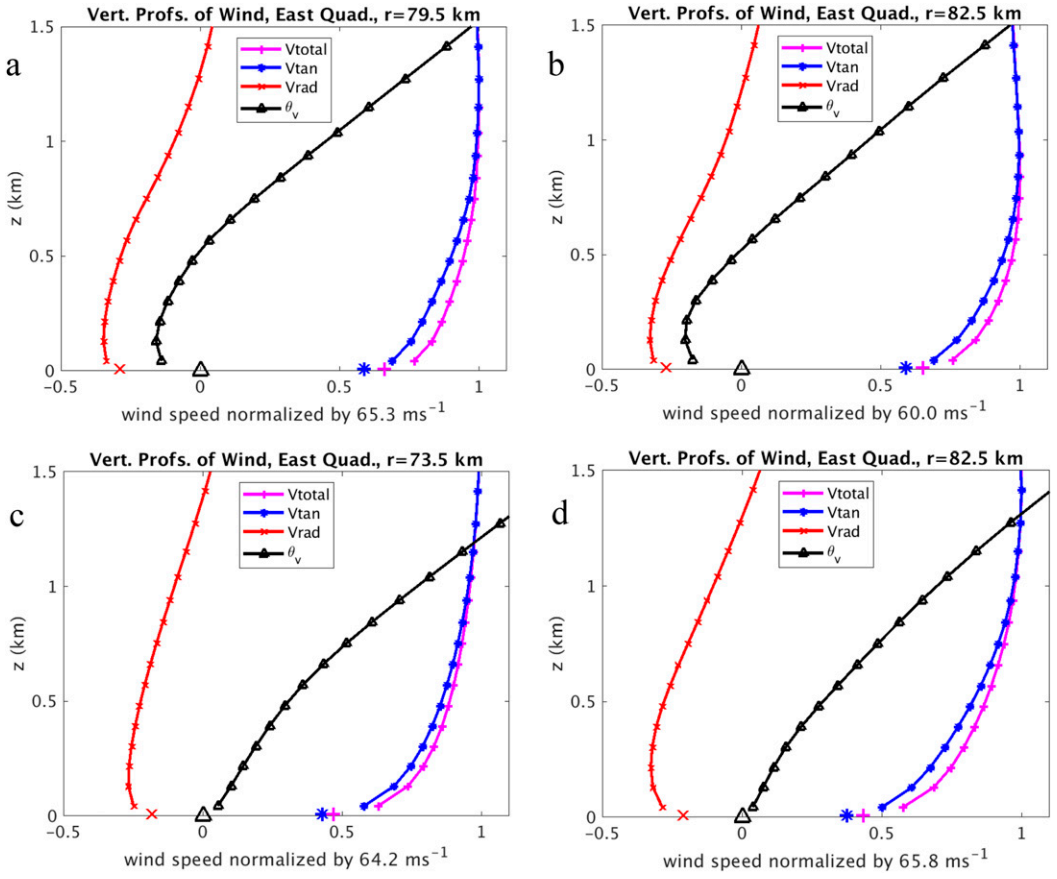

FIG. 13. Azimuthal-mean and time-composited vertical profiles of simulated wind and virtual potential temperature restricted to the quadrants directly east of the center when Wilma was (top) over water (0600–0730 UTC) and (bottom) making landfall (1030–1130 UTC): (a) FinalYSU over water; (b) FinalMYJ over water; (c) FinalYSU at landfall; (d) FinalMYJ at landfall.

open exposure (especially Tower 3), providing an opportunity to evaluate model wind speeds in rough environments.

Along with wind speeds, both Part I and this study evaluated the wind direction in terms of the inflow angle α relative to the cyclone center. Part I showed examples of close similarities and large differences between the azimuthal-mean α and the two synthesized wind analyses, H*WIND and TCSWA. However, both of these have assumptions about α built into their algorithms. In this paper we compared the simulated α at fixed sites directly to observed α. The simulated α were frequently 10° to 20° less than observed. Some of this difference may be due to the fact that there is no adjustment to the wind direction when the models diagnose the 10-m wind from the wind at the lowest model level, the height of which varies closely around 42 m. However, any such error caused by the lack of directional change in the lowest 30–40 m is very small over water. Smith and Montgomery (2013), using the composite dropsonde data of Zhang et al. (2011), find that the change in wind direction between 10 and 50 m is only a few degrees at most (see their Fig. 8). However, over land, Lindvall and Svensson (2019) found that the ERA-Interim reanalyses (Dee et al. 2011) underestimate the surface wind ''turning angle'' almost everywhere around the globe, with differences in the median values mostly ranging from 5° to 10°, depending on factors such as wind speed and surface roughness.

The structure of the hurricane boundary layer over land, and the capability of models to reproduce it, is also of great interest. We attempted to validate the low-level winds in our simulations by comparing them with vertical wind profiles derived from VAD analyses originally produced by G13. By choosing times when the VAD profiles and the simulations had similar intensity, we found some reasonable similarity in the lower boundary layer. Furthermore, the VAD data provided additional information about the temporal evolution of the boundary layer wind speeds at the two locations, KAMX and KBYX, and showed that the two simulations produced similar patterns. With regard to the hurricane boundary layers over both water and land, a clear finding of these studies is that they are extremely similar in the YSU and MYJ schemes.

The accuracies of regional hurricane forecast models have improved substantially over the last decade (Zhang et al. 2015; Marks et al. 2020) and this trend may continue. It may be possible in the not-to-distant future for short-term model forecasts to achieve similar accuracies in terms of track,

intensity, and size as the WRF simulations developed for this study. With additional validation and improvements to the overland wind field, forecast models could directly provide useful information to forecasters, such as the peak wind speeds, the time when they would occur, or the duration of winds of tropical storm or hurricane strength. Such information could be extracted for important sites, such as airports, industry centers, or vulnerable communities, but ultimately we imagine it will be available to the public at any location of their choice.

Acknowledgments. The WRF simulations used in this study were produced and are archived at the University of Miami Institute for Data Sciences and Computing (IDSC). We thank Dr. J. Zhang for providing the H*WIND swath data and Dr. R. Rotunno and two anonymous reviewers for their comments on the paper. Authors D. Nolan and B. McNoldy were supported by the National Science Foundation under the Prediction of and Resilience Against Extreme Events (PREEVENTS) program, Award ICER-1663947.

REFERENCES

Alford, A. A., M. I. Biggerstaff, G. D. Carrie, J. L. Schroeder, B. D. Hirth, and S. M. Waugh, 2019: Near-surface maximum winds during the landfall of Hurricane Harvey. *Geophys. Res. Lett.*, **46**, 973–982, https://doi.org/10.1029/2018GL080013.

——, J. A. Zhang, M. I. Biggerstaff, P. Dodge, F. D. Marks, and D. J. Bodine, 2020: Transition of the hurricane boundary layer during the landfall of Hurricane Irene (2011). *J. Atmos. Sci.*, **77**, 3509–3531, https://doi.org/10.1175/JAS-D-19-0290.1.

Balderrama, J. A., and Coauthors, 2011: The Florida Coastal Monitoring Program (FCMP): A review. *J. Wind Eng. Ind. Aerodyn.*, **99**, 979–995, https://doi.org/10.1016/j.jweia.2011.07.002.

Browning, K. A., and R. Wexler, 1968: The determination of kinematic properties of a wind field using Doppler radar. *J. Appl. Meteor.*, **7**, 105–113, https://doi.org/10.1175/1520-0450(1968)007<0105:TDOKPO>2.0.CO;2.

Bryan, G. H., R. P. Worsnop, J. K. Lundquist, and J. A. Zhang, 2017: A simple method for simulating wind profiles in the boundary layers of tropical cyclones. *Bound.-Layer Meteor.*, **162**, 475–502, https://doi.org/10.1007/s10546-016-0207-0.

Dee, D. P., and Coauthors, 2011: The ERA-Interim reanalysis: Configuration and performance of the data assimilation system. *Quart. J. Roy. Meteor. Soc.*, **137**, 553–597, https://doi.org/10.1002/qj.828.

Fernández-Cabán, P. L., and Coauthors, 2019: Observing Hurricane Harvey's eyewall at landfall. *Bull. Amer. Meteor. Soc.*, **100**, 759–775, https://doi.org/10.1175/BAMS-D-17-0237.1.

Giammanco, I. R., J. L. Schroeder, and M. D. Powell, 2013: GPS dropwindsonde and WSR-88D observations of tropical cyclone vertical wind profiles and their characteristics. *Wea. Forecasting*, **28**, 77–99, https://doi.org/10.1175/WAF-D-11-00155.1.

Hendricks, E. A., B. D. McNoldy, and W. H. Schubert, 2012: Observed inner-core structural variability in Hurricane Dolly (2008). *Mon. Wea. Rev.*, **140**, 4066–4077, https://doi.org/10.1175/MWR-D-12-00018.1.

Hirth, B. D., J. L. Schroeder, C. C. Weiss, D. A. Smith, and M. I. Biggerstaff, 2012: Research radar analysis of the internal boundary layer over Cape Canaveral, Florida, during the landfall of Hurricane Frances (2004). *Wea. Forecasting*, **27**, 1349–1372, https://doi.org/10.1175/WAF-D-12-00014.1.

Hong, S.-Y., Y. Noh, and J. Dudhia, 2006: A new vertical diffusion package with an explicit treatment of entrainment processes. *Mon. Wea. Rev.*, **134**, 2318–2341, https://doi.org/10.1175/MWR3199.1.

Janjić, Z., 1994: The step-mountain eta coordinate model: Further developments of the convection, viscous sublayer, and turbulence closure schemes. *Mon. Wea. Rev.*, **122**, 927–945, https://doi.org/10.1175/1520-0493(1994)122<0927:TSMECM>2.0.CO;2.

Kepert, J. D., 2001: The dynamics of boundary layer jets within the tropical cyclone core. Part I: Linear theory. *J. Atmos. Sci.*, **58**, 2469–2484, https://doi.org/10.1175/1520-0469(2001)058<2469:TDOBLJ>2.0.CO;2.

Knaff, J. A., M. DeMaria, D. A. Molenar, C. R. Sampson, and M. G. Seybold, 2011: An automated, objective, multisatellite platform tropical cyclone surface wind analysis. *J. Appl. Meteor. Climatol.*, **50**, 2149–2166, https://doi.org/10.1175/2011JAMC2673.1.

——, S. P. Longmore, R. T. DeMaria, and D. A. Molenar, 2015: Improved tropical cyclone flight-level wind estimates using routine infrared satellite reconnaissance. *J. Appl. Meteor. Climatol.*, **54**, 463–478, https://doi.org/10.1175/JAMC-D-14-0112.1.

Kosiba, K., J. Wurman, F. J. Masters, and P. Robinson, 2013: Mapping of near-surface winds in Hurricane Rita using fine-scale radar, anemometer, and land-use data. *Mon. Wea. Rev.*, **141**, 4337–4349, https://doi.org/10.1175/MWR-D-12-00350.1.

Landsea, C. W., and J. L. Franklin, 2013: Atlantic hurricane database uncertainty and presentation of a new database format. *Mon. Wea. Rev.*, **141**, 3576–3592, https://doi.org/10.1175/MWR-D-12-00254.1.

Lin, N., J. A. Smith, G. Villarini, T. P. Marchok, and M. Lynn, 2010: Modeling extreme rainfall, winds, and surge from Hurricane Isabel (2003). *Wea. Forecasting*, **25**, 1342–1361, https://doi.org/10.1175/2010WAF2222349.1.

Lindvall, J., and G. Svensson, 2019: Wind turning in the atmospheric boundary layer over land. *Quart. J. Roy. Meteor. Soc.*, **145**, 3074–3088, https://doi.org/10.1002/qj.3605.

Lorsolo, S., J. L. Schroeder, P. Dodge, and F. Marks, 2008: An observational study of hurricane boundary layer small-scale coherent structures. *Mon. Wea. Rev.*, **136**, 2871–2893, https://doi.org/10.1175/2008MWR2273.1.

Marks, F. D., and Coauthors, 2020: National Oceanic and Atmospheric Administration hurricane forecast improvement project years ten to fifteen strategic plan. National Oceanic and Atmospheric Administration Doc., 83 pp., http://www.hfip.org/documents/HFIP_Strategic_Plan_20190625.pdf.

Masters, F. J., P. J. Vickery, P. Bacon, and E. N. Rappaport, 2010: Toward objective, standardized intensity estimates from surface wind speed observations. *Bull. Amer. Meteor. Soc.*, **91**, 1665–1682, https://doi.org/10.1175/2010BAMS2942.1.

Morrison, I., S. Businger, F. Marks, P. Dodge, and J. A. Boosinger, 2005: An observational case for the prevalence of roll vortices in the hurricane boundary layer. *J. Atmos. Sci.*, **62**, 2662–2673, https://doi.org/10.1175/JAS3508.1.

Muramatsu, T., 1986: The structure of a polygonal eye of a typhoon. *J. Meteor. Soc. Japan*, **64**, 913–921, https://doi.org/10.2151/jmsj1965.64.6_913.

Nolan, D. S., and M. T. Montgomery, 2002: Nonhydrostatic, three-dimensional perturbations to balanced, hurricane-like vortices. Part I: Linearized formulation, stability, and evolution. *J. Atmos. Sci.*, **59**, 2989–3020, https://doi.org/10.1175/1520-0469(2002)059<2989:NTDPTB>2.0.CO;2.

——, J. A. Zhang, and D. P. Stern, 2009a: Evaluation of planetary boundary layer parameterizations in tropical cyclones by com-

parison of in situ observations and high-resolution simulations of Hurricane Isabel (2003). Part I: Initialization, maximum winds, and the outer-core boundary layer. *Mon. Wea. Rev.*, **137**, 3651–3674, https://doi.org/10.1175/2009MWR2785.1.

——, D. P. Stern, and J. A. Zhang, 2009b: Evaluation of planetary boundary layer parameterizations in tropical cyclones by comparison of in situ observations and high-resolution simulations of Hurricane Isabel (2003). Part II: Inner-core boundary layer and eyewall structure. *Mon. Wea. Rev.*, **137**, 3675–3698, https://doi.org/10.1175/2009MWR2786.1.

——, J. A. Zhang, and E. W. Uhlhorn, 2014: On the limits of estimating the maximum wind speeds in hurricanes. *Mon. Wea. Rev.*, **142**, 2814–2837, https://doi.org/10.1175/MWR-D-13-00337.1.

——, B. D. McNoldy, and J. Yunge, 2021: Evaluation of the surface wind field over land in WRF simulations of Hurricane Wilma (2005). Part I: Model initialization and simulation validation. *Mon. Wea. Rev.*, **149**, 679–695, https://doi.org/10.1175/MWR-D-20-0199.1.

Pasch, R. J., E. S. Blake, H. D. Cobb III, and D. P. Roberts, 2006: Tropical Cyclone Report: Hurricane Wilma (15–25 October 2005). NHC Tech. Rep. AL252005, 27 pp., https://www.nhc.noaa.gov/data/tcr/AL252005_Wilma.pdf.

Powell, M. D., and S. H. Houston, 1996: Hurricane Andrew's landfall in South Florida. Part II: Surface wind fields and potential real-time applications. *Wea. Forecasting*, **11**, 329–349, https://doi.org/10.1175/1520-0434(1996)011<0329:HALISF>2.0.CO;2.

——, ——, and T. A. Reinhold, 1996: Hurricane Andrew's landfall in South Florida. Part I: Standardizing measurements for documentation of surface wind fields. *Wea. Forecasting*, **11**, 304–328, https://doi.org/10.1175/1520-0434(1996)011<0304:HALISF>2.0.CO;2.

——, ——, L. R. Amat, and N. Morisseau-Leroy, 1998: The HRD real-time hurricane wind analysis system. *J. Wind Eng. Ind. Aerodyn.*, **77–78**, 53–64, https://doi.org/10.1016/S0167-6105(98)00131-7.

Rotunno, R., Y. Chen, W. Wang, C. Davis, J. Dudhia, and G. Holland, 2009: Large-eddy simulation of an idealized tropical cyclone. *Bull. Amer. Meteor. Soc.*, **90**, 1783–1788, https://doi.org/10.1175/2009BAMS2884.1.

Shapiro, L. J., 1983: The asymmetric boundary layer flow under a translating hurricane. *J. Atmos. Sci.*, **40**, 1984–1998, https://doi.org/10.1175/1520-0469(1983)040<1984:TABLFU>2.0.CO;2.

Smith, R. K., and M. T. Montgomery, 2013: On the existence of the logarithmic surface layer in the inner core of hurricanes. *Quart. J. Roy. Meteor. Soc.*, **140**, 72–81, https://doi.org/10.1002/qj.2121.

Stern, D. P., and G. H. Bryan, 2018: Using simulated dropsondes to understand extreme updrafts and wind speeds in tropical cyclones. *Mon. Wea. Rev.*, **146**, 3901–3925, https://doi.org/10.1175/MWR-D-18-0041.1.

Wang, W., J. A. Sippel, S. Arbaca, L. Zhu, B. Liu, Z. Zhang, A. Mehra, and V. Tallapragada, 2018: Improving NCEP HWRF simulations of surface wind and inflow angle in the eyewall area. *Wea. Forecasting*, **33**, 887–898, https://doi.org/10.1175/WAF-D-17-0115.1.

Wingo, S. M. and K. R. Knupp, 2016: Kinematic structure of mesovortices in the eyewall of Hurricane Ike (2008) derived from ground-based dual-Doppler analysis. *Mon. Wea. Rev.*, **144**, 4245–4263, https://doi.org/10.1175/MWR-D-16-0085.1.

Wurman, J., and K. Kosiba, 2018: The role of small-scale vortices in enhancing surface winds and damage in Hurricane Harvey (2017). *Mon. Wea. Rev.*, **146**, 713–722, https://doi.org/10.1175/MWR-D-17-0327.1.

Zhang, J. A., and E. W. Uhlhorn, 2012: Hurricane sea-surface inflow angle and an observation-based parametric model. *Mon. Wea. Rev.*, **140**, 3587–3605, https://doi.org/10.1175/MWR-D-11-00339.1.

——, R. F. Rogers, D. S. Nolan, and F. D. Marks Jr., 2011: On the characteristic height scales of the hurricane boundary layer. *Mon. Wea. Rev.*, **139**, 2523–2535, https://doi.org/10.1175/MWR-D-10-05017.1.

——, D. S. Nolan, R. F. Rogers, and V. Tallapragada, 2015: Evaluating the impact of improvements in the boundary layer parameterization on hurricane intensity and structure forecasts in HWRF. *Mon. Wea. Rev.*, **143**, 3136–3155, https://doi.org/10.1175/MWR-D-14-00339.1.

Zhu, P., 2008: Simulation and parameterization of the turbulent transport in the hurricane boundary layer by large eddies. *J. Geophys. Res.*, **113**, D17104, https://doi.org/10.1029/2007JD009643.